Segmented Mirror Coarse Phasing with a Dispersed Fringe Sensor: Experiment on NGST's Wavefront Control Testbed

Fang Shi[a], Dave Redding[a], Andrew Lowman[a], Chuck Bowers[b], Laura Burns[b], Peter Petrone[b], Catherine Ohara[a], and Scott Basinger[a]

[a]Jet Propulsion Laboratory, California Institute of Technology, Pasadena, CA 91109
[b]Goddard Space Flight Center, NASA, Greenbelt, MD 20771

ABSTRACT

A piston sensing and control algorithm for the segmented mirror coarse phasing using a dispersed fringe sensor (DFS) has been developed for Next Generation Space Telescope (NGST) wavefront sensing and control. The DFS can detect residual piston errors as large as order of a depth-of-focus and can phase the segment mirrors with an accuracy less than 0.1 micron, which is within the capture range of the fine phasing for NGST. A series of experiments has been carried out on the NGST's Wavefront Control Testbed (WCT) to validate the modeling results, evaluate the DFS performance, and systematically explore the factors that affect the DFS performance. This paper reports the testbed results for several critical issues of DFS performance, including DFS dynamic range, accuracy, fringe visibility, and the effects of segment mirror aberrations.

Keywords: Space telescope, segmented mirror, wavefront sensing and control, dispersed fringe sensor

1. INTRODUCTION

Segmented mirror coarse phasing is part of the Next Generation Space Telescope (NGST) wavefront sensing and control (WFS&C) process during the early stage of NGST commissioning [1]. It begins after coarse alignment, the process which includes initial capture, coarse tip-tilt alignment, and focusing of each segmented mirror. After coarse alignment the segmented mirrors are aligned with the residual tilt errors no larger than the a fraction of the point spread function (PSF), which is equivalent to wavefront error of about 0.01 radian in phase, and focused within a depth-of-focus (DOF) of each segmented mirror. Although the residual tilts can be handled by the fine phasing, the residual relative pistons (with amplitudes of ~1 DOF) are still many orders of magnitude too large to be phased by the fine phasing algorithm [2]. Coarse phasing with a dispersed fringe sensor (DFS) provides NGST the wavefront sensing and control of large relative piston errors among the NGST segmented primary mirrors. It reduces the piston errors to within the capture range of fine phasing, the last step in the wavefront sensing and control process [1].

The DFS piston detection algorithms and software were developed using the realistic optical models. Wavefront Control Testbed (WCT) is developed to validate the wavefront sensing and control algorithms developed for the NGST. The WCT provide a flexible testing environment. Since our earlier DFS experiments using the transmissive phase plates [3] and the experiments on the testbed have been concentrated on the DFS piston detection with the segmented mirrors. Various tests have been designed to explore the performance of DFS and influence factors that may affect the DFS performance. In this paper we will report some of the experiment results.

2. DISPERSED FRINGE SENSOR FOR SEGMENTED MIRROR PISTON DETECTION

The DFS uses a transmissive grism in front of the imaging camera as the dispersing element. The grism disperses the light from a broadband source according to its wavelength, forming a spectrum on the camera. The grism deflects the light linearly with wavelength λ along the dispersion direction x:

$$\lambda(x) = \lambda_0 + \frac{\partial \lambda}{\partial x} \cdot x = \lambda_0 + C_0 \cdot x \tag{1}$$

where λ_0 is the central wavelength and C_0 is the linear dispersion rate, which depends on the characteristics of the grism. Coherent addition of the wavefront error due to the relative piston of the segmented mirrors will result in the intensity modulation on the spectrum. The field intensity at any point $E(x)$ along the dispersion is the sum of the fields from the de-phased segments:

$$E(x) = E_1 e^{i(2\pi/\lambda(x)L)} + E_2 e^{i(2\pi/\lambda(x)(L+\delta L))} \tag{2}$$

where E_1 and E_2 are the amplitude of the two segments ($E_1 = E_2$ when they come from two equal area segmented mirrors), L is the diffraction length, and δL is the wavefront optical path length jump due to the piston between the segments. Along the dispersed spectrum, the wavefront may add constructively or destructively, depending on local wavelength and global piston error. Periodic dark bands are formed within the PSF when λ is such that the destruction condition $(2\pi/\lambda) \cdot \delta L = \pi/2$ is met. Along the dispersion direction the fringe intensity pattern has the form:

$$I(x,y) = I_0 \left[1 + \gamma \cdot \cos\left(2\pi \cdot \frac{\delta L}{\lambda(x)} + \phi_0(y) \right) \right] \tag{3}$$

where $I(x,y)$ is the DFS fringe intensity along the dispersion coordinate x, γ is the fringe visibility, and ϕ_0 is a phase constant that depends on where the DFS fringe is extracted – a position along the direction (y) that is perpendicular to the dispersion (x). The intensity of the central row pixels along the dispersion is used as the main DFS signal. It is chosen because it contains the highest signal level. The fringe modulation period is related to the piston error – a larger piston will cause more fringes. The rows above and below the central row also have similar modulations; however, there is a constant phase shift $(\phi_0(y))$ between adjacent rows of pixels. The relative phase shift between these two rows can be used to determine the sign of wavefront piston δL because the lag or lead of the phase shift depends on the sign of the wavefront piston. The DFS fringe analysis software uses all three rows to determine the four parameters in the fringe equation shown in Eq. (3): I_0, γ, ϕ_0, and piston error δL using the least squares method. With the knowledge of the piston value and sign, the executive software can control the actuators to remove the piston error and hence phase the segmented mirrors. When the relative piston error is small, the DFS signal modulation flattens out. Figure xxx shows a WCT DFS fringe image and the extracted DFS signals. A DFS signal with an incomplete modulation cycle over the spectrum may result in erroneous piston detection. However, the small wavefront error δL can still be reliably detected by adding a predetermined piston phase ΔL to the segment being tested so that total wavefront phase error from the piston $P = \Delta L + \delta L$ is large enough to form a DFS signal with some modulations for the DFS analysis software to detect.

The basic requirement for coarse phasing requires that the maximum detectable piston is at least 1 DOF (depth of focus is defined as $DOF = \pm 2\lambda F/\#$, where λ is the wavelength and $F/\#$ is the F-number) of a segmented mirror, and it should bring the piston error down to well within the detection range of fine phasing or the PSF monitoring process which uses the in-focus PSF optimizer (IPO) [7]. As shown in the DFS fringe equation, Eq. (3), the wavelength is linearly dispersed. A larger piston results in denser fringe modulations. For any given piston, the DFS fringe is the densest at the blue wavelength end. Therefore, to reliably detect the piston, the DFS fringe should be resolvable by the detector, which is equivalent to having at least 4 PSFs per fringe cycle. The DFS design is determined by the choice of four parameters: (1) the grism spectral resolution $R_0 = mD/d$, where m is the grating diffraction order, D is the telescope diameter, and d is the grating groove space projected on the sky; (2) the blue end wavelength λ_B; (3) the critical sample wavelength λ_0; and (4) the DFS spectral detector window size N_{pixel}. It is convenient to relate the N_{pixel} with DFS dispersion R_0, blue and red end wavelengths (λ_B and λ_R) as

$$N_{pixel} = 2R_0 \frac{\lambda_R - \lambda_B}{\lambda_0} \tag{4}$$

The relationship with the maximum wavefront piston error δL_{max} requires that at the blue wavelength end, the DFS should be resolved by *4 PSFs*, which is written as

$$\delta L_{max} = \left[\frac{R_0}{4} \left(\frac{\lambda_B}{\lambda_0} \right) + 1 \right] \cdot \lambda_B \tag{5}$$

This requirement defines the grism dispersion power after the wavelength range is determined. When the wavefront piston is large, the blue end of the DFS spectrum may become under-sampled by the DFS. However, we can use only the partial spectrum at the red end where the fringe modulation is still resolved to detect and correct the large wavefront piston error – a process we called the "DFS fringe windowing". DFS fringe windowing will increase the maximum detectable wavefront piston and greatly increase the DFS dynamic range.

3. DFS EXPERIMENTS ON WAVEFRONT CONTROL TESTBED

3.1 DFS Experiment on the Wavefront Control Testbed

The WCT is modular system which consists of (1) the Source Module which can provide both narrow and broad band sources; (2) the Simulator Module which can generate high order aberrations using a 69-actuator deformable mirror (DM) and a wavefront piston using a set of transmissive phase plates, or contains three segmented mirrors that each can be tilted and pistoned individually; (3) the Aft-Optics Module which contains a one-to-one imaging system, a 349-actuator DM for wavefront correction, a flip-in grism, and a CCD camera on a translation stage. The segmented mirrors in the WCT consist of three one-inch diameter spherical mirrors. The segmented mirrors are conjugated to the testbed system aperture which is defined by the Aft-Optical DM. Each segmented mirror is driven by a PZT platform with 3 piezoelectric actuators which provides 12 μm accurate actuation. The PZT platform is mounted on a kinematic mount actuated by picomotors. Compare to the full aperture of DM the three segmented mirror forma sparse aperture with the segmented mirrors cover only about 30% of total aperture area formed by DM. WCT is physically located at Goddard Space Flight Center and most of the experiments are run via the Internet from JPL by the executive software [5]. More detailed information of about the WCT hardware setup and capability can be found in references [4, 6].

The raw DFS signals contain some unwanted spectral features such as DFS grism spectral efficiency, wavelength dependent detector efficiency, source (xenon arc-lamp for WCT testbed or stellar spectra for NGST) which includes sharp emission and absorption lines, and the DFS modulation due to the piston between the segmented mirrors. For the WCT testbed the overall dominant spectral feature in the DFS fringe is the grism efficiency and source lamp emission lines. These unwanted spectral features should be removed before the DFS analysis so that the fringe contains only the modulations caused by the piston. The unwanted spectral features are removed using a calibration spectrum. The so-called calibration spectrum is generated by summing the spectrum intensity across the DFS spectrum. Because modulations caused by the segment piston only appear within the PSF of a single segment, summing across the spectrum removes the spectrum information from the segment piston while leaving all other spectral features, which are only related to the wavelength, in this calibration spectrum. The unwanted spectral features are removed by dividing the raw DFS signal with the normalized calibration spectrum. This forms a clean DFS signal spectrum governed by the relation in Eq. 3. Figure 1 demonstrates this DFS signal processing for the experimental data of WCT.
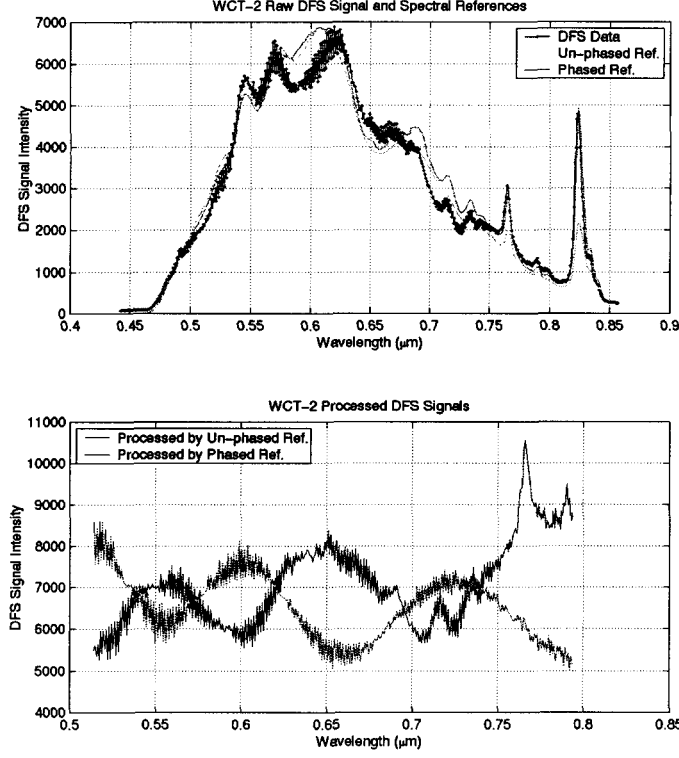
WCT-2 Raw DFS Signal and Spectral References

DFS Data
Un-phased Ref.
Phased Ref.

DFS Signal Intensity

Wavelength (μm)

WCT-2 Processed DFS Signals

Processed by Un-phased Ref.
Processed by Phased Ref.

DFS Signal Intensity

Wavelength (μm)

Figure 1. WCT DFS fringes. Removing the unwanted spectral features for WCT data. *Upper panel*: The raw DFS signal (blue connected dots) and two calibration spectra, one from the unphased segment system (green line) and other from the phased system (red) which gives a better resolution on the sharp line at 820 nm. The DFS signal is buried within the broad spectral features which are dominated by the grism efficiency and spectral lines from the arc lamp. *Lower panel*: The DFS signals after the process removes unwanted spectral features. When using the calibration spectrum from the unphased segments (blue) the sharp lines are not properly removed. The different calibration spectra result in different phases into the DFS signal but have no effect on the piston detection since the absolute phase is irrelevant.

3.2 DFS Piston Error Detection Accuracy

DFS piston accuracy on WCT was studied by both modeling and experiment. The piston detection error ε is defined as the difference between the given piston P_{given} to the segmented mirror and the piston detected $P_{detected}$ by the DFS

$$\varepsilon = P_{given} - P_{detected} \tag{6}$$

Modeling on WCT has shown that the major contribution of DFS piston detection error comes from the uncertainty of the center row position at which the DFS signal is extracted. Furthermore, the fact that the WCT image was under-sampled for the entire spectrum made this effect worse. A multi-trace DFS method has been proposed to solve the problem of the uncertainty in DFS signal row positions. In the multi-trace DFS method, adjacent rows are also extracted as DFS signals as well as the main DFS signal. As in the single-trace method, for each signal an upper and lower row are also used to detect the piston sign. Two predetermined criteria based on the main signal intensity are used to select the signal rows and sign rows. These criteria guarantee that the DFS signals have high enough signal-to-noise ratio. Depending on the PSF size and CCD sampling, the multi-trace may contain three to seven rows of signals for WCT. The detected piston values from each multi-trace signal are selected (weighted) according to the solved I_0 and γ for their quality, and the final piston $P_{detected}$ is derived from the average of all the valid piston detections. Multi-trace DFS can average out the uncertainty errors due to the near-linear relationship between the row positions and the detection errors. Figure 2 shows how multi-trace DFS works and gives an example from the WCT testbed results.
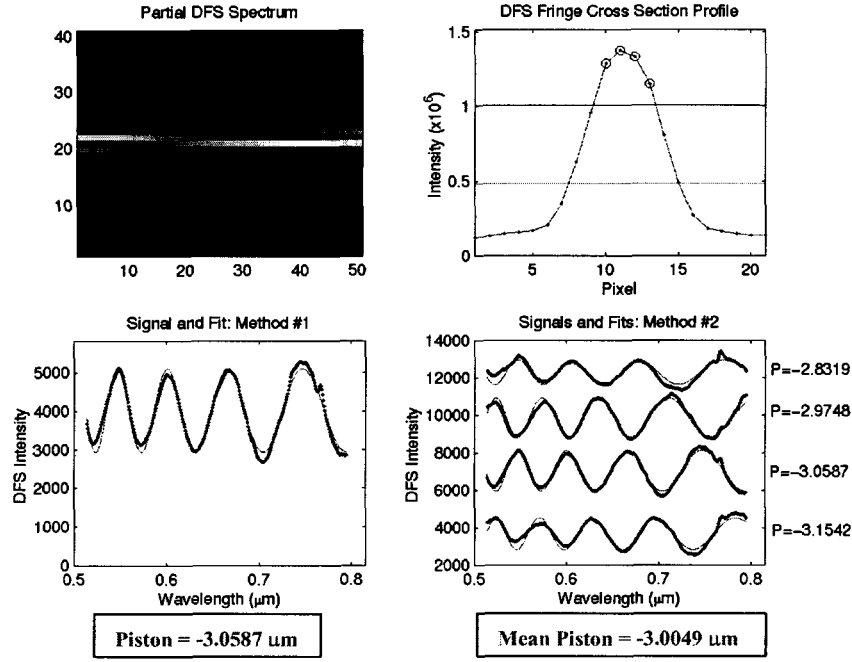
Figure. 2. Single and multi-trace DFS. *Upper left*: a section of the DFS spectrum from WCT displayed in logarithmic scale. *Upper right*: accumulated cross section profile of the spectrum (connected red dots). Rows used for multi-trace signals are indicated by blue circles. The blue horizontal line is the intensity criterion for selection of the signal row and the green line is for the selection of the sign rows. Both criteria must be met for multi-trace DFS signals. *Lower left*: the single-trace DFS signal (blue dots) and its fit (red line). *Lower right*: the multi-trace DFS signals from the same data and their fits. Intensity offsets are added to the traces to separate them in the plot. The fitted piston values show the systematic trend in the pistons detected against the signal row positions.

Modeling on WCT has shown that the multi-trace DFS method is very effective and can reduce the peak-to-valley (P-V) detection error from ~ 0.3 μm to ~ 0.07 μm. An experiment was conducted to test DFS accuracy on the testbed. During the test, pistons of a segmented mirror were scanned through the PZT actuator range (–6 μm to +6 μm) with a known step size. Segmented mirror actuator positions, read from the PZT controller, as well as DFS fringe images were recorded at each piston-scanning step. The single-trace and multi-trace DFS algorithms were then applied to detect the piston from the same DFS fringe images and the detected values were compared with the segment actuator positions. The segmented mirrors used a PZT platform as the actuators to provide segment mirror tip, tilt, and piston. All piezo actuators use the strain gauge sensor to close the loop on actuation position. This mechanism provides the PZT actuator with a sub-nanometer resolution and with repeatability and linearity to 0.03% of the stroke [8] and position accuracy of about < 5 nm. This enabled us to use the PZT position read out to measure the DFS piston detection accuracy. To minimize the long term (~ 1 hour) drift of the testbed, the pistons between adjacent scan steps were compared, i.e., the piston detection error was defined as

$$\Delta P_i = \left| P_{detected}(i) - P_{detected}(i-1) \right| - \left| P_{actuated}(i) - P_{actuated}(i-1) \right| \tag{7}$$

where ΔP_i is the DFS measurement error at the ith scanning step. Plots in Figure 3 summarize the results from the experiment on phasing segment #1 respect to reference segment #2 on WCT. The results show that the multi-trace DFS reduced the scattering of the piston detection errors, and hence increased the accuracy of the detection. The test data have shown that the multi-trace DFS reduced the DFS piston detection error by about a factor of 2, from piston detection error of 50 nm rms and 204 nm peak-to-valley to detection error of 25 nm rms and 89 nm peak-to-valley.
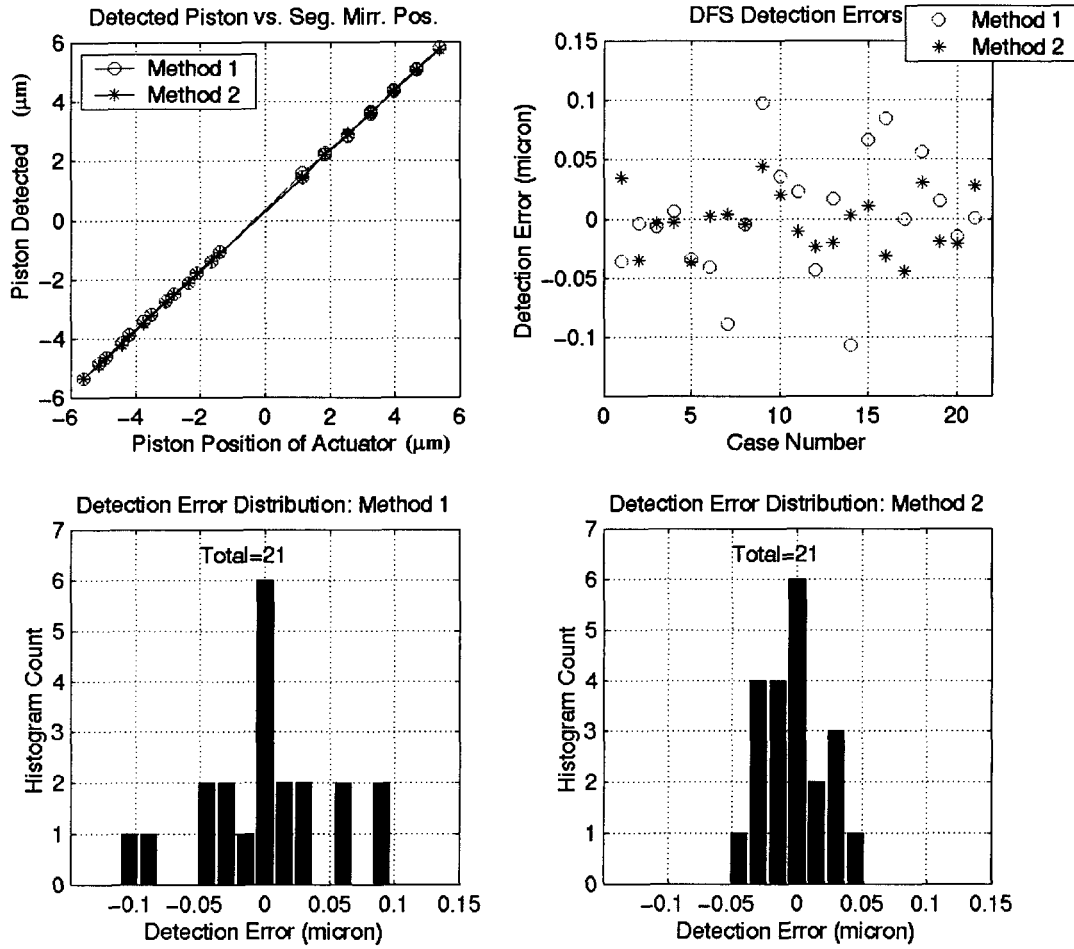
Fig. 3. DFS piston detection accuracy test results. In the plots "Method 1" indicates the single-trace DFS method and "Method 2" multi-trace DFS. *Upper left*: piston detected against piston position readout from the actuators. The line does not cross the zero due to the initial residual piston in the testbed. *Upper right*: piston detection error compared with adjacent piston scans as defined in Eq. 7. *Lower left*: the single-trace DFS piston detection error distribution. *Lower right*: the multi-trace DFS piston detection error distribution. There are total of 21 scan steps used in the plot.

3.3 DFS Piston Error Detection Dynamic Range

The limit of the DFS for detection of large wavefront pistons was tested and modeled on WCT. Because the piezo actuators of the segmented mirror in WCT can only provide a 12-μm stroke, we had to rely on the picomotor stage from New Focus, Inc. in the segmented mirror assembly to generate the large pistons for the segments during the experiment. Figure 4 shows the results from the modeling and experiment. The linearity and repeatability of these picomotor stages are poor so its piston positions readouts are not reliable. However, we used the PZT actuators to add an extra accurate piston on top of the large stroke piston generated by the picomotor as a check for the DFS performance. Since this study was to determine the piston range which the DFS can properly detect (instead of the accuracy), for the experiment we placed the piston positions according to the detection values and put an estimated error bar of ±3 μm on the picomotor position readout (piston given.) From the plots we can see that for both the modeling and experiment, the DFS detection fails around 1 depth-of-focus, which is indicated in the plot by a pair of yellow lines. One of the factors that limit the DFS detection range is that the fringe from WCT is under-sampled for most of the spectral range. The results have also shown that using the partial DFS fringe at the red end of the spectrum can increase the DFS detection range. Results have shown that the experiment and the modeling agree with each other on the DFS detection limits for large piston errors.
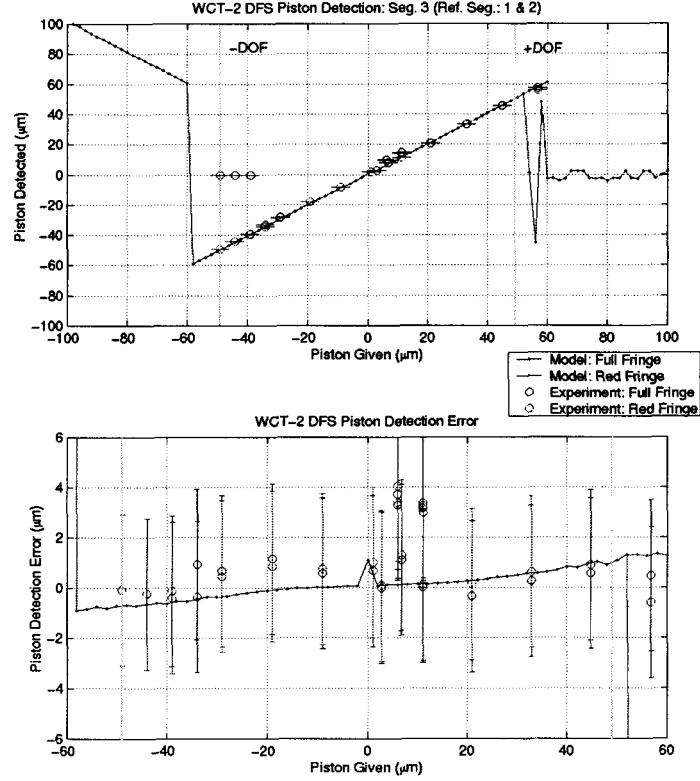
Figure. 4. Results from DFS dynamic range tests from modeling and experiment on WCT. *Upper panel*: piston given versus piston detected. *Lower panel*: the piston detection error versus piston given. An error bar of ±3 μm is given to the picomotor piston readout (upper panel) and shows up as the detection error in the plots on the lower panel for the experiment data. A pair of yellow lines indicates the range of depth-of-focus.

3.4 DFS Fringe Visibility

One of the important characteristics of the DFS fringe is modulation visibility of the fringe which measures the contrast of the modulation. The fringe visibility γ is defined as

$$\gamma = \frac{I_{max} - I_{min}}{I_{mean}} = 2 \times \frac{I_{max} - I_{min}}{I_{max} + I_{min}} \tag{8}$$

where I_{max}, I_{min}, and I_{mean} are the maximum, minimum, and mean DFS signal intensities, respectively. Modeling and experiments have shown that the DFS fringe visibility depends on the relative orientation between the DFS dispersion direction and the direction of the baseline that connects the two segmented mirrors. The DFS fringe modulation is formed by the coherent addition of PSF intensities at each wavelength and dispersive displacement of PSF according to the wavelength. Depending on the relative orientation between the DFS dispersion direction and baseline, the side lobes of the PSF for each wavelength may fill inside the fringe and lower the visibility of the DFS fringe modulation. The highest DFS fringe visibility (contrast) occurs when the DFS disperses the light in the direction that is perpendicular to the baseline between the segments, the orientation at which the side lobes of all the wavelengths are parallel and separated from the main row of the DFS fringe. This orientation effect of the DFS fringe visibility also critically depends on the sparseness of the aperture formed by the segmented mirrors. For the WCT the segmented mirrors form a sparse aperture system which results in its DFS fringe visibility has a stronger relation with the relative orientation of the grism.

The data point obtained form our earlier experiment with the transmissive plate [3] in Figure 5 has demonstrated this effect. The two pistoned half of the transmissive plate forms a full aperture and even at 90° the visibility is still not totally washed out.

Figure 5 shows the WCT experimental results on the relationship between the fringe visibility and the angle between the dispersion and segment baseline. In the experiment, two segments were used and their relative piston was fixed as the grism was rotated at a step size of 5° and a DFS fringe was taken at each grism orientation. The fringes were then analyzed and the fringe visibility was calculated from the fitted solution. We use the fitted signal instead of the raw DFS signal for the fringe visibility calculation to minimize the influence of detector noise. The plots show that the fringe visibility drops quickly to zero and remains at zero when the grism is about 30° away from the highest contrast position. The results also show that, in this test case in which Segment 2 was the reference segment, the visibility against the rotation curve is different when Segment 3 is pistoned up (positive piston) versus pistoned down (negative piston.) Again, we believe this can be explained with the argument from the way that PSF side lobes fill into the fringe.
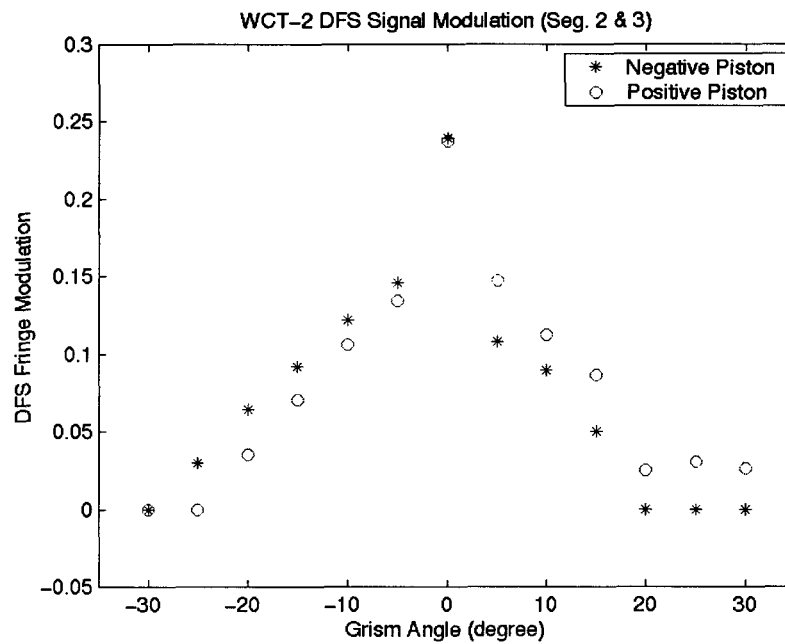

Figure 5. DFS fringe visibility against the rotation angle of the grism. 0° is the position at which the dispersion is perpendicular to the segments' baseline. The test was done for both positive piston (red circles) and negative piston (blue asterisks.) The test has been done for the complete rotation of the grism. The plot only shows the grism angle range from -30° to +30°. Beyond this angular range, the DFS visibility remains at zero. Also shown in the plot are the fringe visibilities from our earlier experiments using the transmissive plates which have full apertures.

3.5 Effect of the Segmented Mirror Surface Aberrations
Segmented mirror aberrations include irregularities on the mirror surface and radius mismatch between the segmented mirrors. First, the wavefront degradation from the mirror surface aberrations results a larger PSF than that of a diffraction-limited PSF. The spreading of PSFs will lower the DFS signal's intensity and visibility therefore lower the DFS signal-to-noise ratio and increase DFS piston detection error. Another effect is that the mirror figure aberration may directly contribute to the error in the measured piston. This is because even if the mean wavefront piston over the segmented mirror is zero, the sub-region wavefront aberration may be picked up as the extra wavefront piston by the DFS, because the DFS signal is extracted from the sub-region of the fringe. However, the multi-trace DFS algorithm described earlier can reduce this effect.

An experiment has been done on WCT to explore the effect of wavefront aberrations on DFS performance. In the experiment, the AODM [4] was used to add the wavefront aberration because the segments and AODM are conjugate to each other. Since the segmented mirrors form a sparse aperture compared with the AODM, the segments only see part of the added aberration. We need to take this into consideration when we calculate how much aberration is really added to the segments. We also need to take out the gross piston from the aberration seen by each segment. Figure 6 shows a typical result from the experiment in which a -1.0 μm Zernike coma was added to the AODM surface. The wavefront aberrations actually seen by the segments have a P-V = 2.6 μm and rms σ = 0.71 μm. The PSF after the segments were realigned is shown in the figure. The plot on the right shows the obtained DFS signal and its fit. There is a ΔP = 0.17 μm detection error compared with the detection when AODM is flat. The experiment shows that DFS detection holds very well against wavefront aberrations. Our test on WCT is limited by the AODM deform capability which, depending on the aberration modes, can only put up to about ±1.2 μm of Zernike aberrations on the DM. Lower-order aberrations were tested, containing up to all third-order aberrations.
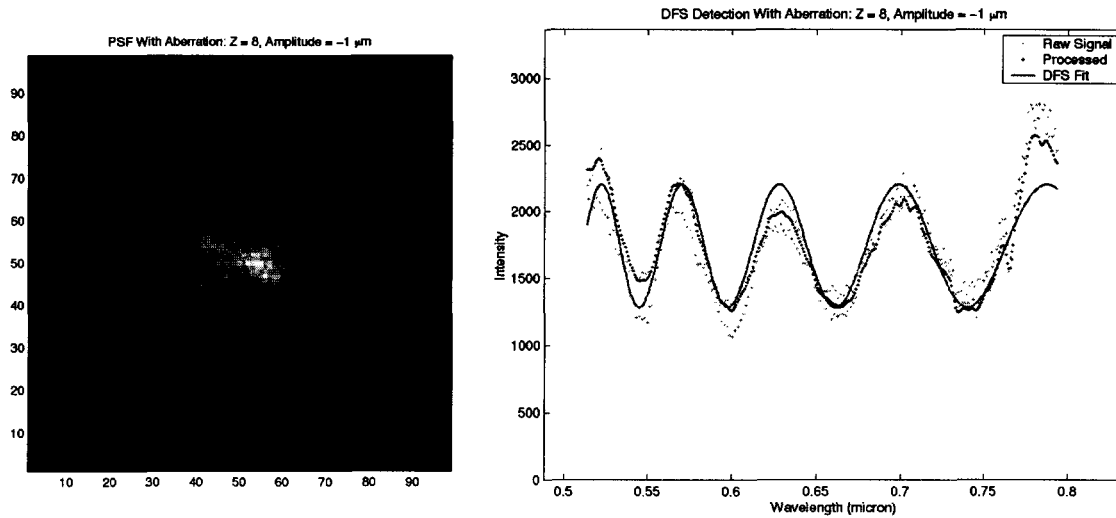

Figure 6. WCT experiment on the effect of segmented mirror surface aberration. PSF on the left is after the segment realignment and shown in logarithmic stretch. The plot one the left shows the raw and processed DFS signal and the DFS piston detection fit to the data.

For the segmented mirror radius mismatch the simulation of WCT has shown that segments can tolerate the up to 0.25% of radius mismatch for visible light. The future update of the WCT will provide capability on the testbed to validate the predicted effect of segments radius mismatch on DFS performance.

Another form of the wavefront error is the line-of-sight jitter and inter-segment jitter. The former is an ensemble of overall wavefront tilt which results in the smear of the DFS fringe, and the latter cause wavefront tilts within each segments and results in the degradation of the co-centering of the segments in which the DFS fringe is forming. Both type of the jittering will lower the DFS visibility and fringe signal intensity therefore lower the DFS signal-to-noise ratio. Detailed studies using models have been done about the jittering effect on DFS performance. The experiment tests on these effects will follow soon.

4. CONCLUSIONS AND FUTURE WORKS

Modeling and experiments on NGST's Wavefront Control Testbed have shown that the dispersed fringe sensor is an effective and accurate method to detect the relative piston error among segmented mirrors. Coarse phasing with the DFS provides the critical middle link in the NGST wavefront sensing and control process. The DFS has a large dynamic range which can sense piston error as large as one or a few depth-of-focus with accuracy a fraction of wavelength. This high dynamic range and good accuracy enables the DFS to correct piston errors too small to be corrected by coarse

alignment but too large to be handled by fine phasing. Because the DFS algorithm uses a least square fit to the fringe to solve a few parameters that govern the fringe equation, the algorithm has high tolerance to unfavorable effects such as jitter, segment misalignment, and mirror figure aberrations, making the DFS a robust coarse phasing algorithm. Compared with other phasing technique, the DFS is very effective. One DFS fringe image normally provides enough information to phase one segmented mirror. Sub-grouping the segments enables multiple fringes in one image which can further reduce the number of images taken and increase the throughput of the coarse phasing process.

The DFS algorithm was developed using realistic models. However, testbed experiments have been critical in developing the DFS algorithm. Applying the DFS algorithm on the testbed helps us to uncover problems when dealing with the real system and makes the idealized algorithm able to handle real system situations. More testbed experiments will follow. The experiments on the WCT testbeds have validated many results from the modeling. Aside environmental uncertainties such as lab seeing and testbed drifts, the experimental results agree with the predictions of models in many aspects. Modeling validation enables us to continue using the realistic optical models to explore system performance, guiding our system design and predicting system performance. As the testbed evolves closer to the real NGST system, the DFS algorithm will also evolve to suit the needs of the system.

Although segment coarse phasing with a DFS is a powerful and efficient method, the algorithm has its limitations. First, the DFS can only sense the relative wavefront piston between segmented mirrors. The DFS cannot sense the relative tilt between the segments, nor can it sense any other low-order wavefront aberrations. However, residual segment tilts can be effectively sensed and corrected by either coarse alignment which uses the image differentiation centroid, more accurately by the in-focus PSF optimizer [7], or by fine phasing which uses the phase retrieval. Second, the accuracy of the DFS is still very coarse and requires fine phasing to further bring down the wavefront error. Third, the DFS fringe contrast depends on the relative orientation between the DFS dispersion and segment baseline as well as depends on the sparseness of aperture. For a multiple segmented system, two grisms, which have dispersion directions perpendicular to each other, may be needed to provide high-contrast fringes for all the possible segment pair combinations.

The experiments have shown that an important factor of DFS detection accuracy is the DFS fringe sampling. PSF under sampling will have an adverse effect on the DFS performance. The PSF sampling issue has shown up in many forms, such as the aperture sparseness and fringe visibility changes against the rotation of grism, in our modeling and experiments. This issue will require further study.

Experiments on WCT are continuing. The WCT testbed is also evolving, adding complexity and approaching higher technology readiness levels by using the flight hardware. These testbed updates will provide more test metrics to validate the models. More experiments will be carried on the new testbed [xxx]. They will provide us with some very rich testing environments and challenges so the DFS algorithm as well as the executive software can be thoroughly tested out before the launch of NGST.

5. ACKNOWLEDGEMENT

6. REFERENCES

[1]   D. Redding, S. Basinger, C. Bowers, R. Burg, L. Burns, D. Cohen, B. Dean, J. Green, A. Loman, C. Ohara, and F. Shi, "Next Generation Space Telescope wavefront sensing and control," SPIE paper 4850-49, Waikoloa, Hawaii (2002).

[2]   D. Redding, S. Basinger, C. Bowers, L. Burns, D. Cohen, B. Dean, P. Dumont, J. Green, A. Loman, C. Ohara, and F. Shi, "Image-based wavefront sensing and control experiment," SPIE paper 4850-62, Waikoloa, Hawaii (2002).

[3] F. Shi, D. Redding, C. Bowers, A. Loman, S. Basinger, T. Norton, P. Petrone, P. Davila, M. Wilson, and R. Boucarut, "DCATT dispersed fringe sensor: modeling and experimenting with the transmissive phase plates," Proc. SPIE 4013, Munich, Germany (2000).

[4] P. Petrone, S. Basinger, C. Bowers, D. Cohen, L. Burns, A. Chu, P. Davila, P. Dogota, B. Dean, J. Green, K. Ha, W. Hayden, D. Lindler, A. Lowman, C. Ohara, D. Redding, F. Shi, M. Wilson, and B. Zukowski, "Optical design and performance of the NGST wavefront control testbed," SPIE paper 4850-55, Waikoloa, Hawaii (2002).

[5] S. Basinger, D. Redding, F. Shi, D. Cohen, J. Green, C. Ohara, A. Lowman, L. Burns, "Wavefront sensing and control software for a segmented space telescope," SPIE paper 4850-56, Waikoloa, Hawaii (2002).

[6] A. Lowman, F. Shi, D. Redding, S. Basinger, C. Bowers, and P. Davila, "Telescope simulator for the DCATT testbed," Proc. SPIE 4013, Munich, Germany (2000).

[7] C. Ohara, D. Redding, F. Shi, and J. Green, "PSF monitoring and in-focus wavefront control for NGST," SPIE paper 4850-64, Waikoloa, Hawaii (2002).

[8] "NanoPosition 1998," Physik Instrumente Catalog, 1998.